ACS APPLIED MATERIALS & INTERFACES

Research Article

www.acsami.org

Facile Approach to Synthesize Au@ZnO Core−Shell Nanoparticles and Their Application for Highly Sensitive and Selective Gas Sensors

Sanjit Manohar Majhi,[†] Prabhakar Rai,[‡] and Yeon-Tae Yu*,[†]

[†]Division of Advanced Materials Engineering and Research Centre for Advanced Materials Development, College of Engineering, Chonbuk National University, Jeonju 561-756, South Korea

[‡]Department of Chemical Engineering, Indian Institute of Technology Kanpur, Kanpur 208016, India

Supporting Information

ABSTRACT: We successfully prepared Au@ZnO core−shell nanoparticles (CSNPs) by a facile low-temperature solution route and studied its gas-sensing properties. The obtained Au@ZnO CSNPs were carefully characterized by X-ray diffraction, transmission electron microscopy (TEM), high-resolution TEM, and UV−visible spectroscopy. Mostly spherical-shaped Au@ZnO CSNPs were formed by 10−15 nm Au NPs in the center and by 40−45 nm smooth ZnO shell outside. After the heat-treatment process at 500 °C, the crystallinity of ZnO shell was increased without any significant change in morphology of Au@ZnO CSNPs. The gas-sensing test of Au@ZnO CSNPs was examined at 300 °C for various gases including H_2 and compared with pure ZnO NPs. The sensor Au@ZnO CSNPs showed the high sensitivity and selectivity to H_2 at 300 °C. The response values of Au@ZnO CSNPs and pure ZnO NPs sensors to 100 ppm of H_2 at 300 °C were 103.9 and 12.7, respectively. The improved response of Au@ZnO CSNPs was related to the electronic sensitization of Au NPs due to Schottky barrier formation. The high selectivity of Au@ZnO CSNPs sensor toward H_2 gas might be due to the chemical as well as catalytic effect of Au NPs.

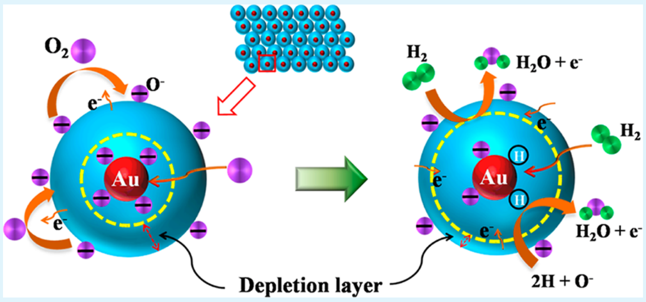

KEYWORDS: *Au@ZnO, core−shell nanoparticles, Schottky junction, sensitivity, H_2*

INTRODUCTION

Owing to the serious concern over the growing environmental pollution and related health effects, considerable research attention has been paid to develop high-performance gas sensors.[1−3] Among various gas sensors, metal oxide semiconductors (MOSs) have been widely researched as promising sensing materials, since they were first proposed by Seiyama et al.[4] in 1962 and a commercial breakthrough was achieved by Naoyoshi Taguchi.[5] These MOSs gas sensors, also known as chemiresistors, are extensively used for monitoring several kinds of hazardous and toxic gases due to their advantages such as simple sensing mechanism, lower maintenance costs, better stability, and facile fabrication.[3,6−8] However, a number of problems, such as high operating temperature and poor selectivity, are also associated with such type of sensors, which needed to be solved to further expand in the fields of gas sensor application. Therefore, it is urgent to find the way to design and engineer novel sensing materials to circumvent these issues.

It is reported that two important key properties of semiconductor device involved in the performance of gas sensors are receptor and transducer functions.[8−10] Hence, it would be an effective way to enhance the performance of gas sensor, especially selectivity, by improving the recognition properties. As a result, several attempts have been made to improve the sensor performance using doping or loading of noble metals. Among them, loading of noble metals over the sensor surface has been recognized as an effective method because the performance of sensors can be enhanced due to their excellent catalytic properties.[11−13] However, noble metals deposited on the surface of the MOSs passivates the surface area involved in gas sensing, and also its use is limited at high working temperature. Because the operation of sensing devices at high working temperatures, these noble metal NPs tend to coagulate and sinter, which leads to the loss of catalytic activity of noble metals.[14] To overcome these problems, a new strategy of core (metal)@shell (oxide semiconductor) nanostructure has been exploited for gas sensors due to their several interesting properties. One of them, in this core−shell nanostructure, the core is isolated from the shell and prevents it from aggregation during sintering at harsh conditions while retaining their individual distinct chemical and physical properties.[15−18] In addition, this core−shell nanostructure exhibits unique and improved functionality as compared to their single-component counterparts.[19] As a result, a number of articles have been reported on such core−shell nanostructures for many potential applications.[20−27] Recently, X. Li et al. reported about the core−shell structured Au@In_2O_3 nano-

Received: January 4, 2015
Accepted: April 22, 2015
Published: April 22, 2015

DOI: 10.1021/acsami.5b00055
ACS Appl. Mater. Interfaces 2015, 7, 9462−9468

composite for the detection of formaldehyde gas. They have used Au@C core−shell NPs as template to deposit the In_2O_3 shell.[27] However, such types of template method require a multistep procedure at high temperature to synthesize the template, and they require high energy consumption. On the other hand, the template-free solution-based methods at lower temperature are facile; therefore, much attention has been paid by many researchers. Thus, one of the specific aims of this work is to synthesize highly sensitive metal@metal-oxide semiconductor core−shell nanostructure materials in a facile and cost-effective way.

Among various semiconductors, zinc oxide (ZnO), which is a well-known n-type semiconductor with a direct wide band gap of 3.37 eV, has been extensively investigated in many potential applications including photocatalytic, field effect transistor, solar cells, chemical sensor, and so on.[28−31] Although a few papers have reported on the gas-sensing performances of ZnO based core−shell nanostructure, a detailed investigation of the role of core metal on sensing property of ZnO is necessary.[32,33] In this work, we present a facile strategy followed by the heat-treatment process to synthesize Au@ZnO core−shell NPs, and their gas-sensing properties are studied. The effect of Au NPs on the sensing performance of Au@ZnO core−shell nanoparticles (CSNPs) was investigated and compared with that of pure ZnO NPs. It was found that the Au@ZnO CSNPs sensor exhibited high H_2 sensitivity and selectivity against other interfering gases (ethanol, acetaldehyde, CO). The detailed experimental results, gas-sensing characteristics, and mechanism of both sensors based on pure ZnO NPs and Au@ZnO CSNPs are explained herein.

■ EXPERIMENTAL DETAILS

Chemicals and Materials. Chloroauric acid ($HAuCl_4 \cdot 4H_2O$,), L-ascorbic acid (AA), and trisodium citrate dihydrate were obtained from Showa Chemicals. Hexamethylenetetramine (HMT), hexadecyltrimethylammonium bromide (CTAB), and zinc nitrate hexahydrate ($Zn(NO_3)_2 \cdot 6H_2O$) were procured from Sigma-Aldrich. All these above chemicals were received as such without any further purification.

Preparation of Au@ZnO Core−Shell Nanoparticles. For the synthesis of Au@ZnO CSNPs, a previous literature method was followed but with some modifications.[34] Typically, calculated amounts of CTAB (6 mM) and AA (3 mM) were added into 60 mL of water and stirred properly for mixing. To this CTAB−AA mixed solution, an equal molar (1:1) amount of $ZnNO_3$ and HMT was added with stirring. The molar ratio of Zn^{2+}/CTAB and AA/Zn^{2+} were taken as 1 and 0.5, respectively. Finally, ∼3 mL of as-prepared 10−15 nm sized Au NPs (see Supporting Information for the synthesis of Au NPs) was dropped into the above mixture solution and stirred for another 5 min before being heated at 85 °C for 8 h in an oven. After that the desired product was centrifuged and washed before being dried at 60 °C for 12 h. After that, the dried powder was collected and heat-treated for 2 h at 500 °C in air. The synthesis of pure ZnO NPs was done according to the same procedure without adding Au colloid.

Characterization. The morphology and microstructural studies of prepared samples were characterized by a TEM (JEM-2010, JEOL) and an HRTEM (Zeiss EM-912, Omega). The selected area electron diffraction (SAED) pattern, high-angle annular dark field scanning TEM (HAADF-STEM) and high-resolution real-time line scan analysis were performed in the HRTEM. The X-ray diffraction (XRD) patterns of all samples were recorded with the help of an X-ray diffractometer (D/Max-2005, Rigaku) having a Cu Kα source (λ =1.541 78 Å). A UV−visible spectroscope (UV-2550, Shimadzu) was used to record the UV−visible spectra.

Sensing Device Fabrication and Measurement. For the sensor device fabrication, ∼0.01g of each sensing material such as pure ZnO NPs and Au@ZnO CSNPs was mixed and ground evenly with one drop of α-terpineol to form a paste, which was painted on the surface of alumina substrates (area: 15 × 15 mm) and then dried at 60 °C. The as-obtained sensor devices were heated at 450 °C for 2 h in air for stabilization and to remove the solvent, before the gas sensing test (Supporting Information, Figure S1: photograph of sensor devices). Both the prepared sensor devices were tested under a temperature-controlled environment at 150−400 °C for different gases such as H_2 (4−100 ppm), ethanol, acetaldehyde, and CO (100 ppm). The total gas flow rate in mass flow controller (MFC) was 100 $cm^3 \cdot min^{-1}$, where the target gas was mixed with nitrogen (background gas) and air (10.5% of oxygen). An Agilent-34970A source meter was used to measure the resistance of the device during the sensor testing. Initially, the resistance of sensor device based on Au@ZnO CSNPs exceeds its limit, that is, above 100 MΩ; therefore, a 10 MΩ resistor was attached to sensor to obtain the actual resistance. The sensor response (R_s) was calculated using (R_a/R_g), where R_a is the sensor resistance in air, and R_g is the resistance measured during the exposure of target gas.

■ RESULTS AND DISCUSSION

Figure 1a is the TEM image of as-synthesized citrate stabilized, spherical-shaped Au NPs having total size ranging from 10 to 15 nm. Figure 1b shows the TEM image of Au@ZnO CSNPs after the ZnO shell coated over Au NPs. Mostly spherical-shaped Au@ZnO CSNPs are formed, and their total sizes are ∼100 ± 10 nm.

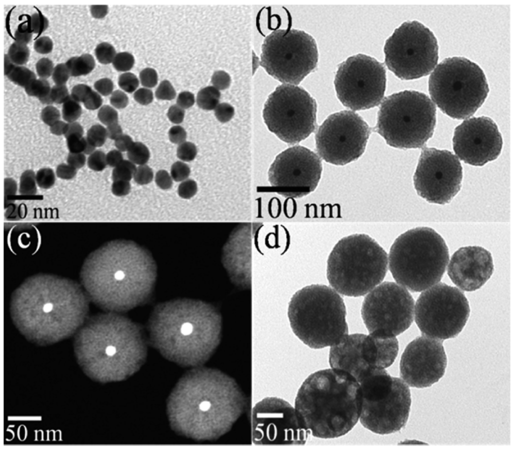

Figure 1. TEM and HAADF-STEM images of (a) Au, (b, c) Au@ZnO core−shell, and (d) pure ZnO NPs.

The thickness of ZnO shell in Au@ZnO CSNPs is measured to be ∼50 ± 5 nm around the 10−15 nm Au NPs. Figure 1c shows the HAADF-STEM image, which was obtained to get a clear picture of the core−shell structure formation. It reveals that Au@ZnO CSNPs are clearly formed by the encapsulation of 10−15 nm Au NPs in the center of 50 ± 5 nm of ZnO shell. In the absence of Au NPs, spherical-shaped ZnO NPs are formed. However, from Figure 1, it was not possible to know the primary particle size of ZnO in prepared nanomaterials because the surface of ZnO shell is very smooth without any granular or crystalline appearance. Since the preparation of sensor devices involved heat-treatment process at 500 °C, the TEM analysis of Au@ZnO CSNPs is therefore also taken after heat-treatment to examine any structural or morphological changes (Figure 2).

Figure 2a depicts the typical TEM image of Au@ZnO CSNPs showing no change in morphology after the heat treatment. The Au NPs are present in the center of core−shell NPs and marked as red color dotted circles and there is no agglomeration and grain growth of Au metal in the Au@ZnO

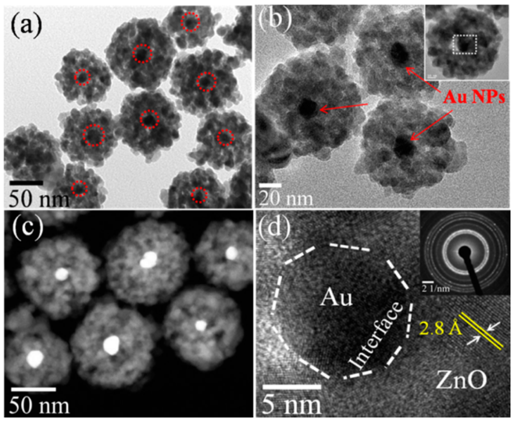

Figure 2. TEM images (a, b); HAADF image (c), and corresponding HRTEM image along with SAED pattern (inset) (d) of Au@ZnO CSNPs after heat treatment at 500 °C for 2h.

CSNPs after heat treatment at 500 °C. From Figure 1, clearly, the shape, total size (100 ± 10 nm), and ZnO shell thickness (50 ± 5 nm) of Au@ZnO CSNPs remain unchanged after heat treatment at such high temperature. However, heat treatment resulted in the increase of crystallinity of ZnO shell, which is composed of ∼15 ± 3 nm primary ZnO NPs. Figure 2b is a high magnification image of Au@ZnO CSNPs, which shows that Au NPs are located in the center of the core−shell nanostructure and looking more contrast and clear as compared to TEM image of Figure 2a. The HAADF image in Figure 2c also confirm about the formation of CSNPs with increased crystallintiy of ZnO shell. The HRTEM image displayed in Figure 2d (taken from the white rectangle area of the single Au@ZnO CSNP in the inset of Figure 2b) is the interface of Au NP and ZnO shell. It shows that the interplanar spacing of ZnO shell is ∼2.8 Å, which is consistent with (100) lattice plane of ZnO. Furthermore, SAED pattern (taken from the single Au@ZnO CSNP present in Figure 2b (inset)) in Figure 2d shows that ZnO shells are polycrystalline in nature. These results indicate the advantage of formation of core−shell NPs, where heat treatment does not result in any morphological change except an increase in crystallinity of ZnO. Figure S2 (Supporting Information) represents a high-resolution real-time line scanning image of Au@ZnO CSNPs, which is analyzed to clarify further the formation of core−shell nanostructure. Figure S2a shows a HAADF-STEM image of two individual Au@ZnO CSNPs from which line-scan is performed. This analysis confirms that all the elements such as Au, Zn, and O are present (Figure S2b−d) in the Au@ZnO CSNPs. It is found that two Au peaks are separated by ∼90 nm, which is equal to ZnO shell thickness (∼45 nm) in two Au@ZnO core−shell NPs (Figure S2b). However, Zn and oxygen peaks are present throughout the spectrum suggesting the continuous presence of ZnO shell (Figure S2b,c). The above study concludes that Au NPs are present inside the center of Au@ZnO CSNPs.

Figure 3a is the TEM image of pure ZnO NPs after heat treatment at 500 °C. It can be observed that such ZnO NPs are also spherical in shape and that the total size is ∼100 ± 40 nm, which consists of 18 ± 4 nm primary ZnO NPs (Figure 3a). Figure 3b shows the SAED pattern of ZnO nanospheres taken from the inset of Figure 3a, and the concentric ring pattern indicates the polycrystalline nature of ZnO NPs.

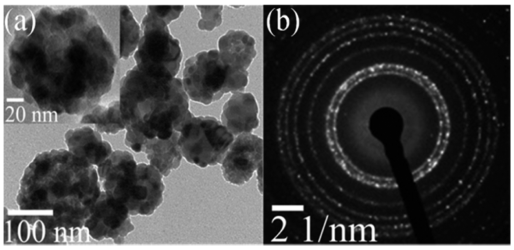

Figure 3. (a) TEM image and (b) corresponding SAED pattern of pure ZnO NPs after heat treatment at 500 °C for 2 h.

XRD study was conducted to examine the crystal structure of prepared materials such as pure ZnO and Au@ZnO CSNPs after heat treatment (Figure 4). From the diffraction pattern of Au@ZnO CSNPs, a small diffraction peak at 38° is indexed to the metallic Au (111) crystal plane (JCPDS 98−000−0230). The remaining peaks in both the specimens are indexed to be wurtzite structure of ZnO (JCPSD 36−1451). However, the inset shows the magnified diffraction pattern of Au diffraction peaks ranging from the angle 37° to 45°, which clearly indicates the Au (111) and Au (222) crystal planes are present at angle 38° and 44.2°, respectively. The XRD study does not indicate any extra phases or impurity peaks in the whole spectrum; therefore, the final obtained products such as pure ZnO and Au@ZnO CSNPs are of high-purity materials. The average crystallite size of the primary ZnO particles in Au@ZnO CSNPs and pure ZnO NPs was calculated to be ∼18.04 and 21.7 nm, respectively, using the Debye−Scherer formula ($D = k\lambda/(\beta \cos \theta)$, where D is the main crystallite size, λ is the wavelength of the X-ray radiation (1.54 Å), k is a constant to be taken as 0.9, β is the full width at half-maximum (fwhm) of the peak, and θ is the diffraction angle.

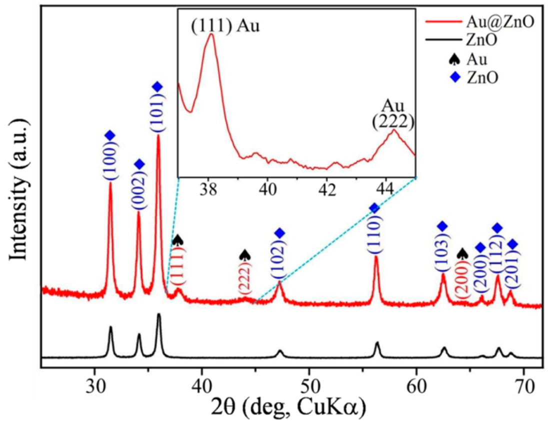

Figure 4. XRD patterns of Au@ZnO CSNPs and ZnO NPs after heat treatment at 500 °C for 2 h.

Figure 5 shows the UV−visible absorption spectra of all the prepared nonmaterial such as Au NPs, pure ZnO NPs, and Au@ZnO CSNPs, respectively. An absorption peak at 522 nm is observed for the 10−15 nm sized Au NPs, which is red-shifted to 584 nm after the ZnO shell formation. This red shift was ascribed to larger refractive index of ZnO shells (2.004) compared to that of water (1.33) indicating the formation of ZnO shells on Au NPs cores. It is interesting to note that the red shift in the absorption peak of Au NPs is increased after the heat treatment. For example, an absorption peak at 534 nm is recorded for as-synthesized Au@ZnO CSNPs sample (Figure

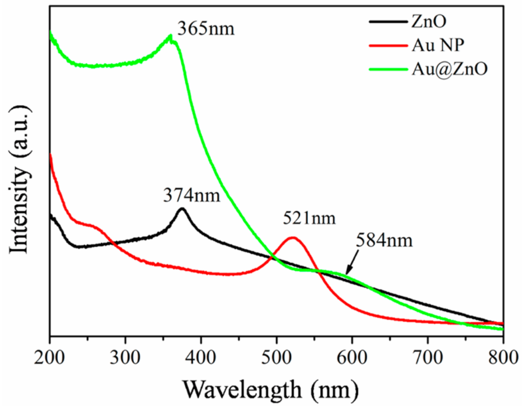

Figure 5. UV−visible absorption spectra of Au, pure ZnO NPs, and Au@ZnO CSNPs.

S3, Supporting Information), which is red-shifted to 584 nm after the heat treatment. This is possibly related to increase of crystallinity as well as refractive index of ZnO shells after the heat-treatment process.[35]

However, the weaker absorption intensity observed for Au NPs in Au@ZnO CSNPs may be due to the thick ZnO shell formation. Furthermore, the ZnO characteristic peak at 365 nm is recorded for Au@ZnO CSNPs, which is broadened and also blue-shifted compared to pure ZnO NPs (374 nm). The calculated band gap of ZnO in pure ZnO and Au@ZnO CSNPs was 3.31 and 3.39 eV, respectively. The reason for the blue shift of ZnO peak in Au@ZnO CSNPs may be due to the interaction of Au core and ZnO shell.[36] Furthermore, the primary ZnO particle size in Au@ZnO CSNPs is smaller compared to pure ZnO NPs, which may also be one of the reasons behind the blue shift in absorption band of ZnO in Au@ZnO CSNPs.

■ GAS-SENSING POPERTIES

The response of metal oxide semiconductor gas sensors usually depend on the operating temperature. Therefore, as an important factor, it is necessary to examine the optimum operating temperature of all the prepared sensor devices. Both the sensors such as pure ZnO NPs and Au@ZnO CSNPs were tested at different temperatures from 150 to 400 °C for 100 ppm of H_2 gas, the results of which are shown in Figure 6a. Initially, as the operating temperature was raised the response of both sensors increased and reached maximum at 300 °C to 100 ppm of H_2. However, when the operating temperature was increased further to 400 °C, the responses decreased gradually for both sensors. The response values of Au@ZnO CSNPs sensor (R_s = 103.9) was 8 times higher than that of pure ZnO NPs (R_s = 12.7) at 300 °C for 100 ppm of H_2. Hence, 300 °C is the optimum working temperature in this work, and further gas-sensing measurements were performed at this temperature.

The response-recovery transients of sensors based on pure ZnO NPs and Au@ZnO CSNPs for H_2 target gas (4−100 ppm) at 300 °C is shown in Figure 6b. Usually, n-type semiconductor gas sensors, when exposed to reducing gases environment, the resistance amplitude of the sensor decreases and increases again when exposed to air atmosphere. In Figure 6b, both of the sensors show similar kind of characteristics, that is, decrease of the resistances when they are exposed to H_2. However, the baseline resistance of Au@ZnO CSNPs sensor is higher as compared to that of pure ZnO NPs sensor, and the reason for this was discussed in the Gas-Sensing Mechanism Section. The response and recovery times are also considered as important parameters for any gas-sensing devices. The response time is the time needed for a sensing device to reach 90% of total resistance change after the supply of H_2 gas (adsorption), whereas the recovery time is the 90% of resistance change to return to its original position after H_2 gas stopped followed by the supply of air (desorption). The

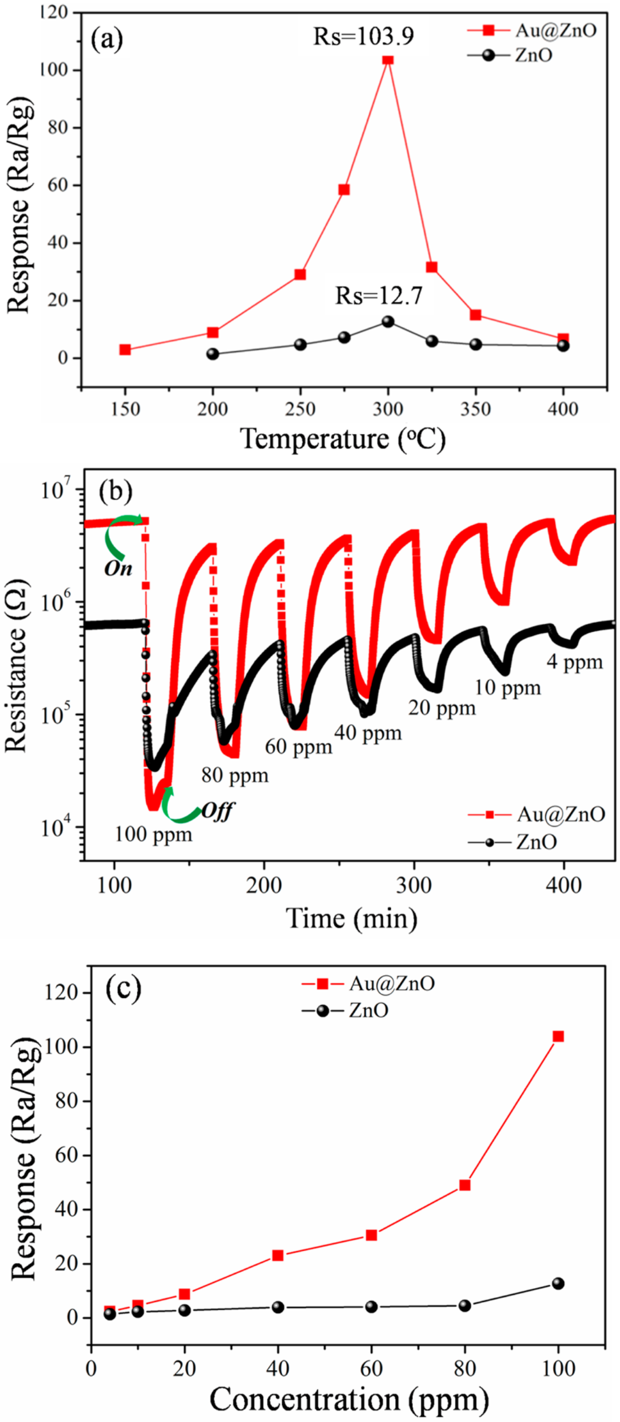

Figure 6. (a) Responses vs operating temperature of pure ZnO and Au@ZnO CSNPs sensors to 100 ppm of H_2. (b) Dynamic H_2 response-recovery transients of both the sensors at 300 °C. (c) Responses vs H_2 concentrations plot of pure ZnO NPs and Au@ZnO CSNPs sensors at 300 °C.

response time of the Au@ZnO CSNPs sensor to 100 ppm of H_2 was calculated to be 75 s (Figure 6b), whereas the recovery time was relatively longer, that is, 600 s. The response time of pure ZnO NPs sensor (Figure 6b) for 100 ppm of H_2 was 121 s, whereas recovery time was too long. Figure 6c shows the H_2 gas concentration versus response graph of the sensors such as pure ZnO NPs and Au@ZnO CSNPs measured at 300 °C. From the graph, it is found that Au@ZnO CSNPs sensor exhibits higher response value at each concentration as compared to pure ZnO NPs. Starting from the lower to higher concentrations of H_2, the responses of pure ZnO NPs and Au@ZnO CSNPs sensor were calculated and plotted in Figure 6c. The response values of Au@ZnO CSNPs to 4, 10, 20, 40, 60, 80, and 100 ppm of H_2 were 2.43, 4.6, 8.7, 23, 30.5, 49, and 103.9, respectively, whereas the response values of pure ZnO NPs were 1.4, 2.28, 2.8, 3.9, 4.1, 4.5, and 12.7, respectively. Also, the sensing performances of both the sensors were tested at parts per billion level of H_2 concentration, which is shown in Figure S4 (see Supporting Information). The H_2 responses of Au@ZnO CSNPs and pure ZnO NPs to 500 ppb were ∼1.12 and 1.0, respectively. However, below 500 ppb of H_2 gas none of the sensors shows any response. Figure S5 (see Supporting Information) shows the reproducibility test of pure ZnO NPs and Au@ZnO CSNPs sensors at 400 °C. Response of both sensors was examined by conducting the sensing test for repeating three cycles to 100 ppm of H_2, and it was found that both devices show good reproducibility and stability when alternatively exposed to air and H_2.

Selectivity in gas sensing is another important parameter that is needed for a real-time practical application. Figure 7 displays the selectivity test of both the sensing devices such as pure ZnO NPs and Au@ZnO CSNPs. Their responses were evaluated by testing with other interfering gases such as H_2, ethanol, acetaldehyde, and CO with a concentration of 100 ppm at 300 °C. It is shown from Figure 7 that, for all gases, the Au@ZnO CSNPs sensor exhibited enhanced responses as compared to pure ZnO NPs. However, Au@ZnO CSNPs shows high selectivity to H_2 among other interfering gases indicating that the Au@ZnO CSNPs has a better ability to discriminate H_2 gas. The above results confirmed the role of Au NPs in gas sensor in terms of improvement of sensitivity and selectivity.

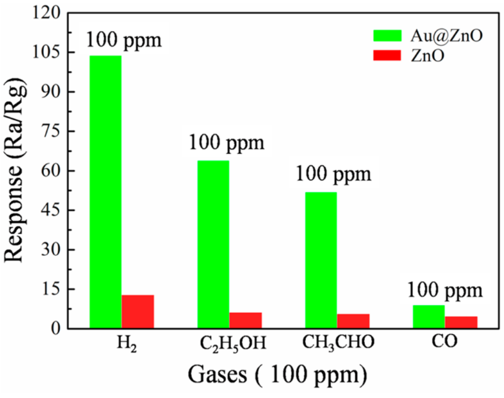

Figure 7. Responses vs different reducing gases plot for pure ZnO and Au@ZnO CSNPs to 100 ppm of various gases at 300 °C.

■ GAS-SENSING MECHANISM

The mechanism behind the H_2 sensing performances of both the sensors such as pure ZnO NPs and Au@ZnO CSNPs can be explained on the basis of well-established sensing mechanism of n-type semiconducting gas sensors, which is reported in many previous papers.[37−39] Initially when the air is supplied to pure ZnO sensor, the oxygen molecules in air adsorb on the surface of ZnO semiconductor and capture its conduction-band electrons to form ionic species of oxygen (O_2^-, O^-, O^{2-}). Therefore, a depletion layer (ΔL) is formed on the ZnO sensor surface (as shown in Figure 8a-1), which eventually causes an increase of resistance in ZnO sensor (Figure 6b).[38] As soon as the target gas (H_2) is supplied, the chemisorbed oxygen ions react with H_2 gas and return the trapped electrons to ZnO sensor. As a result, the resistance of ZnO sensor decreases. The relevant reactions are written as follows:[39]

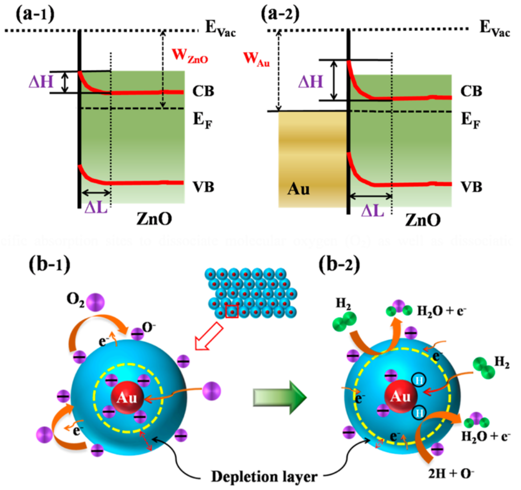

Figure 8. A schematic illustration of (a) energy-band diagram of ZnO and Au@ZnO CSNPs; (b) gas-sensing reaction of Au@ZnO CSNPs sensor under the air and target gas condition.

$$H_{2(gas)} \leftrightarrow H_{2(ads)} \tag{1}$$

$$H_{2(ads)} + O^{-}{}_{(ads)} \leftrightarrow H_2O_{(gas)} + e^{-} \tag{2}$$

$$H_{2(ads)} + O^{2^{-}}{}_{(ads)} \leftrightarrow H_2O_{(gas)} + 2e^{-} \tag{3}$$

Mainly two sensitization effects such as electronic and chemical sensitization are involved for the improved gas-sensing performance of Au@ZnO CSNPs compared to that of pure ZnO NPs.[40−43] Au NPs played a significant role in enhancing the gas-sensing performance and was involved in both the mechanisms. The electronic sensitization mechanism is responsible for the high response (sensitivity) of Au@ZnO CSNPs sensor as compared to that of pure ZnO NPs. The presence of Au NPs in this Au@ZnO core−shell composite will form a typical metal−semiconductor Schottky junction between Au NPs and ZnO shells.[43,44] As Au metal (5.1 eV) has greater work function than ZnO (4.65 eV), more electrons will be transferred from the conduction band of ZnO shell to Au core than to the pure ZnO NPs. Therefore, the energy band of ZnO results In a greater bending at the Au@ZnO interface with a broad depletion layer (Figure 8a-2).[42] This is also supported from the high baseline resistance of Au@ZnO CSNPs as compared to that of ZnO NPs. When the Au@ZnO CSNPs sensor tested under the target gas, the H_2 gas molecules get oxidized by reacting with adsorbed oxygen ions and resulted in free electrons (eqs 2 and 3), which returned to ZnO. This leads to the lowering of width of electron depletion layer, and hence the resistance decreases in Au@ZnO core−shell NPs, improving the response. Since the response (R_s) is measured by R_a/R_g for reducing gases, with higher R_a value for Au@ZnO CSNPs there will be higher response.

However, the chemical sensitization mechanism is responsible for the high selectivity of Au@ZnO CSNPs toward H_2 gas. It is known that Au NP is a good catalyst and serves as specific absorption site to dissociate molecular oxygen (O_2) as well as dissociation and ionization of H_2 molecules into H atoms due to spillover effect (as shown in Figure 8b-2).[37,41−43,45−47] Therefore, more oxygen gets adsorbed and captures free electrons to form oxygen ionic species. Also adsorption of H_2 molecules via Au catalyst is faster and readily oxidized by reacting with the oxygen ionic species (O^-), which release water and free electron (e^-) as products. As a result, the resistance of Au@ZnO CSNPs sensor decreases, and response increases. The H_2 and O_2 spillover reactions on Au surfaces are presented below:

$$2\mathrm{Au} + \mathrm{H}_{2(\mathrm{gas})} \rightarrow 2\mathrm{Au/H} \tag{4}$$

$$2\mathrm{H} + \mathrm{O}^-_{(\mathrm{ads})} \rightarrow \mathrm{H_2O}_{(\mathrm{vap})} + e^- \tag{5}$$

$$2\mathrm{Au} + \mathrm{O}_{2(\mathrm{gas})} \rightarrow 2\mathrm{Au/O} \tag{6}$$

$$\mathrm{O} + e^- \rightarrow \mathrm{O}^-_{(\mathrm{ads})} \tag{7}$$

Thus, it is clear from the results obtained in this work that the Au NPs are reliable sensitizers and good catalyst for enhancing the sensing reactions, resulting high sensitivity, selectivity, and response/recovery time in Au@ZnO core−shell NPs. However, the decrease of responses at higher temperatures (above 300 °C) is attributed to dominating desorption process of H_2 molecules rather than faster adsorption.[48] On the other hand, at lower temperatures sensor shows low responses, which may be due to less thermal energy, sluggish diffusion, and surface reactions of H_2 gas molecules with oxygen ionic species.[49,50]

CONCLUSIONS

In summary, the Au@ZnO CSNPs sensor was prepared via a facile solution approach and demonstrated its gas-sensing performance against pure ZnO NPs sensor. The formation of a typical core@shell structure was confirmed by different studies such as TEM, HAADF-STEM, and UV−visible optical spectroscope. The Au@ZnO CSNPs sensor exhibited significantly improved gas-sensing performances as compared to that of pure ZnO NPs for all interfering gases. Here, Au NPs catalyst plays the determining role for improving the performance of Au@ZnO CSNPs sensor. The Au@ZnO CSNPs sensor showed the high response (R_s = 103.9), rapid response time (75 s), and high selectivity to H_2 at 300 °C. Also, both pure ZnO NPs and Au@ZnO CSNPs sensors were able to detect H_2 even at sub-parts per million level (500 ppb) with responses of 1.0 and 1.12, respectively. The improved sensing performances with regard to sensitivity and selectivity of Au@ZnO CSNPs sensor were attributed to both electronic and chemical sensitization effects of Au NPs. Thus, it is believed that the developed Au@ZnO CSNPs hybrid structure might be further used as a promising gas-sensing material.

ASSOCIATED CONTENT

Ⓢ Supporting Information

Information about the preparation of Au NPs. Photographs of sensor devices made from ZnO NPs and Au@ZnO CSNPs. HR-TEM line scan images of Au@ZnO CSNPs. UV−visible spectra of as-synthesized Au@ZnO CSNPs. Dynamic H_2 response-recovery transients of pure ZnO and Au@ZnO CSNPs (500 ppb−2 ppm) at 300 °C. Response reproducibility test of the ZnO and Au@ZnO CSNPs sensors at 400 °C. The Supporting Information is available free of charge on the ACS Publications website at DOI: 10.1021/acsami.5b00055.

AUTHOR INFORMATION

Corresponding Author

*E-mail: yeontae@jbnu.ac.kr. Phone: +82-63-270-2288. Fax: +82-63-270-2305.

Notes

The authors declare no competing financial interest.

ACKNOWLEDGMENTS

The authors are thankful to Ministry of Education and Human Resource Development and National Research Foundation (NRF) for the financial support through the BK21 plus program by Korea Government under Project MEST-NRF-2010-0019626. Centre for University Research Facility (CURF), CBNU, and KBSI, Jeonju branch are acknowledged for the analysis of TEM and HR-TEM, respectively.

REFERENCES

(1) Vellejos, S.; Khatko, V.; Calderer, J.; Gracia, I.; Cane, C.; Llobet, E.; Correig, X. Micro-Machined WO_3-Based Sensors Selective to Oxidizing gases. *Sens. Actuators, B* **2008**, *132*, 209−215.

(2) Liu, X.; Cheng, S.; Liu, H.; Hu, S.; Zhang, D.; Ning, H. Review: A Survey On Gas Sensing Technology. *Sensors* **2012**, *12*, 9635−9665.

(3) Stoychevaa, T.; Annanoucha, F. E.; Gracia, I.; Llobet, E.; Blackman, C.; Correig, X.; Vellejos, S. Micro Machined Gas Sensors Based On Tungsten Oxide Nanoneedles Directly Integrated Via Aerosol Assisted CVD. *Sens. Actuators, B* **2014**, *198*, 210−218.

(4) Seiyama, T.; Kato, A.; Fujiishi, K.; Nagatani, N. A New Detector for Gaseous Components Using Semiconductive Thin Films. *Anal. Chem.* **1962**, *34*, 1502−1503.

(5) Taguchi, N. A Metal Oxide Gas Sensor. Japanese Patent No. 45−38200, 1962.

(6) Korotcenkov, G. Review: Metal Oxides For Solid-State Gas Sensors: What Determines Our Choice? *Mater. Sci. Eng., B* **2007**, *139*, 1−23.

(7) Sun, Y.-F.; Liu, S.-B.; Meng, F.-L.; Liu, J.-Y.; Jin, Z.; Kong, L.-T.; Liu, J.-H. Metal Oxide Nanostructures and Their Gas Sensing Properties: A Review. *Sensors* **2012**, *12*, 2610−2631.

(8) Rai, P.; Kwak, W.-K.; Yu, Y. T. Solvothermal Synthesis of ZnO Nanostructures and Their Morphology-Dependent Gas-Sensing Properties. *ACS Appl. Mater. Interfaces* **2013**, *5*, 30126−3032.

(9) Yamazoe, N.; Sakai, G.; Shimanoe, K. Oxide Semiconductor Gas Sensors. *Catal. Surv. Asia* **2003**, *7*, 63−75.

(10) Majhi, S. M.; Rai, P.; Raj, S.; Chon, B.-S.; Park, K.-K.; Yu, Y. T. Effect of Au Nanorods on Potential Barrier Modulation in Morphologically Controlled $Au@Cu_2O$ Core−Shell Nanoreactors for Gas Sensor Applications. *ACS Appl. Mater. Interfaces* **2014**, *6*, 7491−7497.

(11) Liu, X.; Zhang, J.; Guo, X.; Wang, S.; Wu, S. Core-Shell α-$Fe_2O_3@SnO_2$/Au Hybrid Structures and Their Enhanced Gas Sensing Properties. *RSC Adv.* **2012**, *2*, 1650−1655.

(12) Chang, S. J.; Hsueh, T. J.; Chen, I. C.; Hsieh, S. F.; Chang, S. P.; Hsu, C. L.; Lin, Y. R.; Huang, B. R. Highly Sensitive ZnO Nanowire

Acetone Vapor Sensor with Au Adsorption. *IEEE Trans. Nanotechnol.* **2008**, *7*, 754−759.

(13) Liu, X. W.; Wang, F. Y.; Zhen, F.; Huang, J. R. In Situ Growth of Au Nanoparticles on the Surfaces of Cu_2O Nanocubes for Chemical Sensors with Enhanced Performance. *RSC Adv.* **2012**, *2*, 7647−7651.

(14) Arna, P. M.; Comotti, M.; Schuh, F. High-Temperature-Stable Catalysts by Hollow Sphere Encapsulation. *Angew. Chem., Int. Ed.* **2006**, *45*, 8224−8227.

(15) Rai, P.; Majhi, S. M.; Yu, Y.-T.; Lee, J.-H. Synthesis of Plasmonic Ag@SnO_2 Core-Shell Nanoreactors for Xylene Detection. *RSC Adv.* **2015**, *5*, 17653−17657.

(16) Wu, X. F.; Song, H. Y.; Yoon, J. M.; Yu, Y. T.; Chen, Y. F. Synthesis of Core−Shell Au@TiO_2 Nanoparticles with Truncated Wedge-Shaped Morphology and Their Photocatalytic Properties. *Langmuir* **2009**, *25*, 6438−6447.

(17) Kim, Y. S.; Rai, P.; Yu, Y. T. Microwave Assisted Hydrothermal Synthesis of Au@TiO_2 Core-Shell Nanoparticles for High Temperature CO Sensing Applications. *Sens. Actuators, B* **2013**, *186*, 633−639.

(18) Yu, Y. T.; Dutta, P. Examination of Au/SnO_2 Core-Shell Architecture Nanoparticle for Low Temperature Gas Sensing Applications. *Sens. Actuators, B* **2011**, *157*, 444−449.

(19) Zhang, N.; Liu, S.; Xu, Y. J. Recent Progress on Metal Core@ Semiconductor Shell Nanocomposites as a Promising Type of Photocatalyst. *Nanoscale* **2012**, *4*, 2227−2238.

(20) Haldar, K. K.; Patra, A. Fluorescence Enhancement and Quenching of Eu^{3+} Ions by Au-ZnO Core-Shell and Au Nanoparticles. *Appl. Phys. Lett.* **2009**, *95*, 063103−3.

(21) Haldar, K. K.; Sen, T.; Patra, A. Au@ZnO Core-Shell Nanoparticles Are Efficient Energy Acceptors with Organic Dye Donors. *J.Phys.Chem.C* **2008**, *112*, 11650−11656.

(22) Kuo, C. H.; Hua, T. E.; Huang, M. H. Au Nanocrystal-Directed Growth of Au−Cu_2O Core−Shell Heterostructures with Precise Morphological Control. *J. Am. Chem. Soc.* **2009**, *131*, 17871−17878.

(23) Qi, J.; Chen, J.; Li, G.; Li, S.; Gao, Y.; Tang, Z. Facile Synthesis of Core−Shell Au@CeO_2 Nanocomposites with Remarkably Enhanced Catalytic Activity for CO Oxidation. *Energy Environ. Sci.* **2012**, *5*, 8937−8941.

(24) Jiang, W.; Zhou, Y.; Zhang, Y.; Xuan, S.; Gong, X. Superparamagnetic Ag@Fe_3O_4 Core-Shell Nanospheres: Fabrication, Characterization and Application as Reusable Nanocatalysts. *Dalton Trans.* **2012**, *41*, 4594−4601.

(25) Hang, S.; He, J.; Wang, J.; Zhang, S. Y.; Liu, C.; Sritharan, T.; Mhaisalkar, S.; Han, M. Y.; Wang, D.; Chen, H. Investigating the Multiple Roles of Polyvinylpyrrolidone for a General Methodology of Oxide Encapsulation. *J. Am. Chem. Soc.* **2013**, *135*, 9099−9110.

(26) Song, M. K.; Rai, P.; Ko, K. J.; Jeon, S. H.; Chon, B. S.; Lee, C. H.; Yu, Y. T. Synthesis of TiO_2 Hollow Spheres by Selective Etching of Au@TiO_2 Core-Shell Nanoparticles for Dye Sensitized Solar Cell Applications. *RSC Adv.* **2014**, *4*, 3529−3535.

(27) Li, X.; Liu, J.; Guo, H.; Zhou, X.; Wang, C.; Sun, P.; Hu, X.; Lu, G. Au@In_2O_3 Core-Shell Composites: A Metal−Semiconductor Heterostructure for Gas Sensing Applications. *RSC Adv.* **2015**, *5*, 545−551.

(28) Pradhan, G. K.; Martha, S.; Parida, K. M. Synthesis of Multifunctional Nanostructured Zinc−Iron Mixed Oxide Photocatalyst by a Simple Solution-Combustion Technique. *ACS Appl. Mater. Interfaces* **2012**, *4*, 707−713.

(29) Suh, D. I.; Lee, S. Y.; Hyung, J. H.; Kim, T. H.; Lee, S. K. Multiple ZnO Nanowires Field-Effect Transistors. *J.Phys.Chem.C* **2008**, *112*, 1276−1281.

(30) Tian, J.; Lv, L.; Wang, X.; Fei, C.; Liu, X.; Zhao, Z.; Wang, Y.; Cao, G. Microsphere Light-Scattering Layer Assembled by ZnO Nanosheets for the Construction of High Efficiency (>5%) Quantum Dots Sensitized Solar Cells. *J. Phys.Chem.C* **2014**, *118*, 16611−16617.

(31) Rai, P.; Jeon, S. H.; Lee, C. H.; Lee, J. H.; Yu, Y. T. Functionalization of ZnO Nanorods by CuO Nanospikes for Gas Sensor Applications. *RSC Adv.* **2014**, *4*, 23604−23609.

(32) Li, X.; Zhou, X.; Liu, Y.; Sun, P.; Shimanoe, K.; Yamazoe, N.; Lu, G. Microwave Hydrothermal Synthesis and Gas Sensing Application of Porous ZnO Core-Shell Microstructures. *RSC Adv.* **2014**, *4*, 32538−32543.

(33) Chung, F.-C.; Zhu, Z.; Luo, P.-Y.; Wu, R.-J.; Li, W. Au@ZnO Core-Shell Structure for Gaseous Formaldehyde Sensing at Room Temperature. *Sens. Actuators, B* **2014**, *199*, 314−319.

(34) Yang, Y.; Han, S.; Zhou, G.; Zhang, L.; Li, X.; Zou, C.; Huang, S. Ascorbic-Acid-Assisted Growth of High Quality M@ZnO: A Growth Mechanism and Kinetics Study. *Nanoscale* **2013**, *5*, 11808−11819.

(35) Zheng, Y. B.; Huang, T. J.; Desai, A. Y.; Wang, S. J.; Tan, L. K.; Gao, H.; Huan, A. C. H. Thermal Behavior of Localized Surface Plasmon Resonance of Au/TiO_2 Core/Shell Nanoparticle Arrays. *Appl. Phys. Lett.* **2007**, *90*, 183117−3.

(36) Sun, L.; Wei, G.; Song, Y.; Liu, Z.; Wang, L.; Li, Z. Solution-Phase Synthesis of Au@ZnO Core-shell Composites. *Mater. Lett.* **2006**, *60*, 1291−1295.

(37) Wang, Z. J.; Wang, W.; Liu, Y. L. Enhanced Acetone Sensing Performance of Au Nanoparticles Functionalized Flower-Like ZnO. *Sens. Actuators, B* **2012**, *168*, 39−45.

(38) Kaneti, Y. V.; Yue, J.; Jiang, X.; Yu, A. Controllable Synthesis of ZnO Nanoflakes with Exposed $(10\bar{1}0)$ for Enhanced Gas Sensing Performance. *J. Phys. Chem. C* **2013**, *117*, 13153−13162.

(39) Sadek, A. Z.; Choopun, S.; Wlodarski, W.; Ippolito, S. J.; Kourosh, K. Characterization of ZnO Nanobelt-Based Gas Sensor for H_2, NO_2, and Hydrocarbon Sensing. *IEEE Sens. J.* **2007**, *7*, 919−924.

(40) Matsushima, S.; Teraoka, Y.; Miura, N.; Yamazoe, N. Electronic Interaction Between Metal Additives and Tin Dioxide in Tin Dioxide-Based Gas Sensors. *Jpn. J. Appl. Phys.* **1998**, *27*, 1798−1802.

(41) Shim, Y. S.; Zhang, L.; Kim, D. H.; Choi, Y. R.; Nahm, S. H.; Kang, C. Y.; Lee, W.; Jang, H. W. Highly Sensitive and Selective H_2 and NO_2 Gas Sensors Based on Surface-Decorated WO_3 Nanoigloos. *Sens. Actuators, B* **2014**, *198*, 294−301.

(42) Wang, L.; Dou, H.; Lou, Z.; Zhang, T. Encapsuled Nanoreactors (Au@SnO_2): A New Sensing Material for Chemical Sensors. *Nanoscale* **2013**, *5*, 2686−2691.

(43) Li, X.; Liu, J.; Guo, H.; Zhou, X.; Wang, C.; Sun, P.; Hu, X.; Lu, G. Au@In_2O_3 Core-Shell Composites: Metal-Semiconductor Heterostructure for Gas Sensing Applications. *RSC Adv.* **2015**, *5*, 545−551.

(44) Wang, Y.; Lin, Y.; Jiang, D.; Li, F.; Li, C.; Zhu, L.; Wen, S.; Ruan, S. Special Nanostructure Control of Ethanol Sensing Characteristics Based on Au@In_2O_3 Sensor with Good Selectivity and Rapid Response. *RSC Adv.* **2015**, *5*, 9884−9890.

(45) Vellejos, S.; Umek, P.; Stoycheva, T.; Annanouch, F.; Llobet, E.; Correig, X.; Marco, P. D.; Bittencourt, C.; Blackman, C. Single-Step Deposition of Au- and Pt-Nanoparticle-Functionalized Tungsten Oxide Nanoneedles Synthesized via Aerosol-Assisted CVD, and Used for Fabrication of Selective Gas Microsensor Arrays. *Adv. Funct. Mater.* **2013**, *23*, 1313−1322.

(46) Xiang, Q.; Meng, G. F.; Zhao, H. B.; Zhang, Y.; Li, H.; Ma, W. J.; Xu, J. Q. Au Nanoparticle Modified WO_3 Nanorods with Their Enhanced Properties for Photocatalysis and Gas Sensing. *J.Phys.Chem.C* **2010**, *114*, 2049−2055.

(47) Guo, J.; Zhang, J.; Zhu, M.; Ju, D.; Xu, H.; Cao, B. High-Performance Gas Sensor Based on ZnO Nanowires Functionalized by Au Nanoparticles. *Sens. Actuators, B* **2014**, *199*, 339−345.

(48) Rakshit, T.; Santra, S.; Manna, I.; Ray, S. K. Enhanced Sensitivity and Selectivity of Brush-Like SnO_2 Nanowires/ZnO Nanorod Heterostructure Based Sensors For Volatile Compounds. *RSC Adv.* **2014**, *4*, 36749−36756.

(49) Chang, J. F.; Kuo, H. H.; Leu, I. C.; Hon, M. H. The effects of Thickness and Operation Temperature on ZnO:Al thin film CO Gas Sensor. *Sens. Actuators, B* **2002**, *84*, 258−264.

(50) Shinde, V. R.; Gujar, T. P.; Lokhande, C. D. Enhanced Response of Porous ZnO Nanobeads Towards LPG: Effect of Pd Sensitization. *Sens. Actuators, B* **2007**, *123*, 701−706.